Wind and Structures, *Vol. 17, No. 1(2013) 001-019*
DOI:http://dx.doi.org/10.12989/was.2013.17.1.001

Multiscale finite element method applied to detached-eddy simulation for computational wind engineering

Yue Zhang, Rooh A. Khurram* and Wagdi G. Habashi

NSERC-J.-Armand Bombardier Industrial Research Chair for Multi-disciplinary Analysis and Design of Aerospace Systems CFD Lab, Department of Mechanical Engineering, McGill University Montreal, QC, Canada H3A 2S6

(Received November 19, 2011, Revised April 16, 2012, Accepted April 30, 2012)

Abstract. A multiscale finite element method is applied to the Spalart-Allmaras turbulence model based detached-eddy simulation (DES). The multiscale arises from a decomposition of the scalar field into coarse (resolved) and fine (unresolved) scales. It corrects the lack of stability of the standard Galerkin formulation by modeling the scales that cannot be resolved by a given spatial discretization. The stabilization terms appear naturally and the resulting formulation provides effective stabilization in turbulent computations, where reaction-dominated effects strongly influence near-wall predictions. The multiscale DES is applied in the context of high-Reynolds flow over the Commonwealth Advisory Aeronautical Council (CAARC) standard tall building model, for both uniform and turbulent inflows. Time-averaged pressure coefficients on the exterior walls are compared with experiments and it is demonstrated that DES is able to resolve the turbulent features of the flow and accurately predict the surface pressure distributions under atmospheric boundary layer flows.

Keywords: multiscale method; detached-eddy simulation; computational wind engineering; inflow turbulence generation; CAARC model

1. Introduction

The Computational Wind Engineering (CWE) community applies Computational Fluid Dynamics (CFD) techniques to analyze and model wind-structure related phenomena such as building aerodynamics and aeroelastics, pedestrian-level wind environment, transport and dispersion of air pollutants in urban environment, and so on. Since wind is turbulent in nature, CWE thus deals with three-dimensional, time-dependent stochastic flows, causing turbulence modeling in CWE applications to encounter special challenges. Murakami (1998) ascribed these challenges to four aspects: high Reynolds numbers, complex flow field, sharp edges of bluff bodies, and inflow and outflow boundary conditions. In traditional Reynolds-Averaged Navier-Stokes (RANS) methods, mean flow fields of turbulence can be computed via a time-averaged form of the Navier-Stokes equations, but the unknown nonlinear Reynolds stress terms, which represent the fluctuating turbulent effects, are modeled by additional equations. Even though RANS has achieved much success in predicting mean flow solutions, it is not able to

*Corresponding author, Dr., E-mail: RoohUlAmin.Khurram@KAUST.EDU.SA

http://www.techno-press.org/?journal=was&subpage=8 ISSN: 1226-6116 (Print), 1598-6225 (Online)

satisfy the demand for instantaneous turbulence resolutions and dynamic wind loads exerted on structures. In Large Eddy Simulation (LES), the large eddies are resolved explicitly and the small eddies are modeled by subgrid-scale models. However, one issue confronting LES is that very fine grids in three dimensions must be placed in the boundary layers to accurately represent turbulence structures in the near-wall regions, which dramatically increases the computational cost for high Reynolds numbers. While LES is a powerful research tool, it is not yet suitable to produce numerical results in a timeframe and at a cost comparable to wind tunnels.

Detached-eddy simulation (DES), first proposed by Spalart *et al.* (1997), is an increasingly popular hybrid RANS/LES technique able to predict, at an affordable cost, massively separated flows at high Reynolds number. Therefore, the idea is to treat the entire boundary layers by RANS models and separated regions by LES models. The application of DES in the field of CWE is slowly increasing. Haupt *et al*. (2011) applied DES and zonal DES to predict the atmospheric flow over surface mounted cube. The results for pressure coefficients showed that DES, and particularly zonal DES, matched the full-scale measurements better than the RANS solutions. Mannini *et al.* (2011) carried out a comprehensive study of DES to a 5:1 rectangular cylinder and demonstrated that DES gave good agreement with experiments in terms of Strouhal number, C_D and C_L. These results suggest that DES is suitable for high Reynolds number bluff body aerodynamics, for which the cost of LES may be prohibitive.

One important requirement of CWE is to accurately compute wall shear stresses. However, as the reaction terms dominate the turbulent behavior in the boundary layer, the stability of numerical simulation may be hard to control and therefore lead to inaccurate results. In this paper we extend the multiscale based stabilized finite element formulation for the Spalart-Allmaras (S-A) turbulence model, as presented in Khurram and Habashi (2011), to DES. Stabilized finite element methods are formed by adding to the standard Galerkin method variational terms that are mesh-dependent, consistent and numerically stabilizing (Brooks and Hughes 1982, Franca *et al.*1998, Hughes *et al.* 1989, Tezduyar and Sathe 2007, Tezduyar *et al.* 2009). Hughes (1995) revisited the origins of the stabilization schemes from a variational multiscale approach. In the Hughes' variational multiscale method, different stabilization techniques appear as special cases of the underlying subgrid-scale modeling concept. Taking this line of thought, which is based on the notion of the existence of fine scales in the problem, various stabilized formulations have been proposed for the advection-diffusion equation (Masud and Khurram 2004), the incompressible Navier–Stokes equations (Masud and Khurram 2006), and for fluid-structure interaction problems (Khurram and Masud 2006).

In order to validate the multiscale DES in predicting surface pressure distributions on tall buildings, the Commonwealth Advisory Aeronautical Research Council (CAARC) standard tall building model is chosen in the present work. Comprehensive aerodynamic and aeroelastic behavior of CAARC building model have been widely researched via several wind tunnel experiments. Melbourne (1980) compared the averaged and standard deviation of surface pressure according to the database from six wind tunnel centers. The pressure discrepancies were attributed to the difference in approaching longitudinal velocity spectrum and blockage ratios. Tanaka and Lawen (1986) carried out a pressure and aeroelastic study of CAARC with a small geometric scale of 1:1000, and showed that no particular error was observed due to the extremely small geometric scale. Goliger and Milford (1988) investigated the sensitivity of geometric scale and turbulence intensity, and found that geometric scale had negligible influence, but that turbulence intensity had a more noticeable effect on the response of the building. Obasaju (1992) provided a complete study of mean and standard deviation, as well as the spectra of forces and base overturning

moments of CAARC under both uniform and atmospheric boundary layer flows. In addition, a computational study of CAARC was conducted by Huang *et al*. (2007) using RANS and LES. They found that the velocity profile of inflow mainly influenced the mean pressure distribution on the walls of the building, but that turbulence intensity had a significant effect on the fluctuating forces. Braun and Awruch (2009) conducted a numerical study for aerodynamic and aeroelastic behavior of CAARC using a fluid-structure interaction technique.

The inlet boundary condition is an important issue for DES and LES. In contrast to RANS simulations where only mean flow quantities are imposed at the inlet boundary, LES and DES also need the fluctuating parts of inflow. The inflow turbulence generation was considered one of the three key numerical issues for LES in CWE, as well as other CFD applications (Tamura 2008). It is a tough problem, first because inflow turbulence should satisfy several important characteristics of high Reynolds number natural wind, such as mean velocity, turbulence intensity, spatial correlation, power spectrum density and so on. Moreover, the inflow turbulence generation techniques should be easy to modify according to various wind environments, simple to implement in CFD codes, and compatible with the Navier-Stokes equations. Currently, there are two main approaches taken. The first is precursor or recycling/rescaling methods, which require an auxiliary computational domain to drive the turbulence and then introduce it to the main domain. Some success is achieved in CWE applications (Kataoka 2008, Nozawa and Tamura 2002), but a drawback is the difficulty in controlling turbulence characteristics and the additional computational cost of the precursor. The second category of inflow turbulence generation is synthesized methods, in which instantaneous artificial velocities, following prescribed turbulence features, are generated separately and then imposed at the inlet. As no external domain is required, it is much less expensive than precursor or recycling/rescaling methods. Moreover, turbulence features are simpler to modify for different flow conditions. The most challenging problem of the synthesized methods is that the artificial velocity fields must satisfy the divergence-free condition. Recently a promising synthesized inflow turbulence generation method labeled discretizing and synthesizing random flow generation (DSRFG) (Huang *et al*. 2010) has demonstrated how to simulate a spatially correlated turbulent flow field.

To the best of the authors' knowledge, the present work is a first attempt to employ DES for predicting surface pressure distributions of tall buildings under atmospheric boundary layer flows. The DES formulation is based on the S-A turbulence model equations and discretized by multiscale finite element method. The multiscale DES is then applied to the CAARC tall building model with Reynolds number of 94,000. Comparisons are demonstrated between URANS with uniform inflow, DES with uniform inflow, and DES with turbulent inflow in terms of time-averaged surface pressure coefficient distribution. Instantaneous velocity magnitude contours and three-dimensional streamlines are exhibited as well.

2 Numerical strategies

2.1 Strong form of Spalart-Allmaras turbulence model based DES

The strong form of normalized Spalart-Allmaras (S-A) turbulence model (Spalart and Allmaras 1994) is

$$\begin{aligned}&\frac{\partial \nu_E}{\partial t}+u_j\frac{\partial \nu_E}{\partial x_j}-C_{b1}\tilde{S}\nu_E+C_{w1}f_w\frac{1}{\mathrm{Re}_\infty}\left(\frac{\nu_E}{d}\right)^2\\&\quad-\frac{1}{\sigma\,\mathrm{Re}_\infty}\left(\frac{\partial}{\partial x_k}\left(\left(\nu+\nu_E\right)\frac{\partial \nu_E}{\partial x_k}\right)+C_{b2}\frac{\partial \nu_E}{\partial x_k}\frac{\partial \nu_E}{\partial x_k}\right)=0\end{aligned} \tag{1}$$

The terms appearing in (1) are: time derivative of ν_E, convective term, production term, destruction term, and diffusion term, respectively. ν_E is a working variable and turbulent eddy viscosity is determined by $\nu_T=\nu_E f_{v1}$. The modified magnitude of vorticity is

$$\tilde{S}=S+\frac{1}{\mathrm{Re}_\infty}\frac{\nu_E}{\kappa^2 d^2}f_{v2},\quad S=\sqrt{2\Omega_{ij}\Omega_{ij}},\quad \Omega_{ij}=\frac{1}{2}\left(\frac{\partial u_i}{\partial x_j}-\frac{\partial u_j}{\partial x_i}\right) \tag{2}$$

and d is the distance to the nearest wall. The functions f_{v1} and f_{v2} are defined as

$$f_{v1}=\frac{\chi^3}{\chi^3+C_{v1}^3},\quad f_{v2}=1-\frac{\chi}{1+\chi f_{v1}} \tag{3}$$

where $\chi=\frac{\nu_E}{\nu}$ with ν the laminar viscosity. The destruction term is formed with

$$f_w=g\left(\frac{1+C_{w3}^6}{g^6+C_{w3}^6}\right)^{\frac{1}{6}},\quad g=r+C_{w2}\left(r^6-r\right),\quad r=\frac{\nu_E}{\kappa^2 d^2\,\mathrm{Re}_\infty S+\nu_E f_{v2}} \tag{4}$$

The closure coefficients of the model are

$$\begin{aligned}&C_{b1}=0.1355,\ C_{b2}=0.622,\ C_{v1}=7.1,\ \sigma=\frac{2}{3}\\&C_{w1}=\frac{C_{b1}}{\kappa^2}+\frac{\left(1+C_{b2}\right)}{\sigma},\ C_{w2}=0.3,\ C_{w3}=2,\ \kappa=0.41.\end{aligned} \tag{5}$$

Based on S-A equations, the DES formulation is obtained by replacing d in the destruction term and production term with $\tilde{d}=\min\left(d,C_{DES}\Delta_{\max}\right)$, where C_{DES} is suggested to be 0.65 and $\Delta_{\max}$ is the largest dimension of the local element (Spalart *et al*. 1997).

2.2 Linearized weak form of DES formulation

First, the temporal discretization of DES formulation is performed, using a standard backward Euler scheme. The semi-discrete form of DES formulation is

$$\frac{\nu_E^{n+1}}{\Delta t}+\left[u_j\frac{\partial \nu_E}{\partial x_j}-C_{b1}\tilde{S}\nu_E+C_{w1}f_w\frac{1}{\mathrm{Re}_\infty}\left(\frac{\nu_E}{\tilde{d}}\right)^2 -\frac{1}{\sigma\,\mathrm{Re}_\infty}\left(\frac{\partial}{\partial x_k}\left(\left(\nu+\nu_E\right)\frac{\partial \nu_E}{\partial x_k}\right)+C_{b2}\frac{\partial \nu_E}{\partial x_k}\frac{\partial \nu_E}{\partial x_k}\right)\right]^{n+1}=\frac{\nu_E^n}{\Delta t} \tag{6}$$

where n and n+1 are the time levels and Δt is the time step. In order to keep the presentation simple, we drop the superscript n+1 from here on. Using w as the weighting function, the linearized weak form of (6) can be shown as

$$\begin{aligned}&\left(w,\frac{\Delta \nu_E}{\Delta t}\right)_{\Omega^e}+\left(w\,u_j\frac{\partial \Delta \nu_E}{\partial x_j}\right)_{\Omega^e}-\left(w\,C_{b1}\tilde{S}\Delta \nu_E\right)_{\Omega^e}\\&+\left(w,\,C_{w1}f_w\frac{\nu_E}{\mathrm{Re}_\infty\tilde{d}^2}\Delta \nu_E\right)_{\Omega^e}+\left(\frac{\partial w}{\partial x_k},\frac{1}{\sigma\,\mathrm{Re}_\infty}\left(\nu+\nu_E\right)\frac{\partial \Delta \nu_E}{\partial x_k}\right)_{\Omega^e}\\&-\left(w,\frac{2C_{b2}}{\sigma\,\mathrm{Re}_\infty}\frac{\partial \nu_E}{\partial x_k}\frac{\partial \Delta \nu_E}{\partial x_k}\right)_{\Omega^e}=\left(w,\frac{\nu_E^n}{\Delta t}-R\right)_{\Omega^e}\end{aligned} \tag{7}$$

where $(\bullet,\bullet)=\int_{\Omega^e}(\bullet)\,\mathrm{d}\Omega^e$ i.e., L_2 product of the indicated arguments over domain Ω^e, $\Delta\nu_E$ is the incremental value in the Newton iteration and R, shown below, is the residual at iteration i.

$$R=\left[\frac{\nu_E}{\Delta t}+u_j\frac{\partial \nu_E}{\partial x_j}-C_{b1}\tilde{S}\nu_E+\frac{C_{w1}f_w}{\mathrm{Re}_\infty}\left(\frac{\nu_E}{\tilde{d}}\right)^2 -\frac{1}{\sigma\,\mathrm{Re}_\infty}\left(\frac{\partial}{\partial x_k}\left(\left(\nu+\nu_E\right)\frac{\partial \nu_E}{\partial x_k}\right)+C_{b2}\frac{\partial \nu_E}{\partial x_k}\frac{\partial \nu_E}{\partial x_k}\right)\right]_i \tag{8}$$

2.3 Multiscale method

We assume an overlapping sum decomposition of the scalar field into coarse scales or resolvable scales and fine scales or subgrid scales.

$$\nu_E(\boldsymbol{x})=\underbrace{\overline{\nu}_E(\boldsymbol{x})}_{\text{coarse scale}}+\nu'_E(\boldsymbol{x}) \tag{9}$$

Likewise, we assume an overlapping sum decomposition of the weighting function into the coarse and the fine scale components indicated as $\overline{w}$ and w', respectively.

$$w(\boldsymbol{x})=\underbrace{\overline{w}(\boldsymbol{x})}_{\text{coarse scale}}+w'(\boldsymbol{x}) \tag{10}$$

Substituting the additive decomposition of solution and weighting function into the weak form (7) and exploiting the linearity of the weighting function, we get a coarse scale problem and a fine scale problem. Modeling of the fine scale solution via approximate solution of the fine scale problem and substitution of the fine scale solution into the coarse scale problem, yields the multiscale form, which is shown as

$$
\begin{aligned}
&(w, a_i \frac{\partial \Delta\nu_E}{\partial x_i}) + (\frac{\partial w}{\partial x_i}, k \frac{\partial \Delta\nu_E}{\partial x_i}) + (w, s\Delta\nu_E) \\
&+(a_i \frac{\partial w}{\partial x_i}, a_j \frac{\partial \Delta\nu_E}{\partial x_j}) + (a_i \frac{\partial w}{\partial x_i}, \tau a_j \frac{\partial \Delta\nu_E}{\partial x_j}) + (a_i \frac{\partial w}{\partial x_i}, \tau s\Delta\nu_E) \\
&+(k \frac{\partial}{\partial x_i}\frac{\partial w}{\partial x_i}, a_j \frac{\partial \Delta\nu_E}{\partial x_j}) + (k \frac{\partial}{\partial x_i}\frac{\partial w}{\partial x_i}, \tau a_j \frac{\partial \Delta\nu_E}{\partial x_j}) + (k \frac{\partial}{\partial x_i}\frac{\partial w}{\partial x_i}, \tau s \frac{\partial \Delta\nu_E}{\partial x_i}) \\
&-(sw, a_j \frac{\partial \Delta\nu_E}{\partial x_j}) + (sw, \tau a_j \frac{\partial}{\partial x_j}\frac{\partial \Delta\nu_E}{\partial x_j}) - (sw, \tau s\Delta\nu_E) \\
&= (w, f) + (a_i \frac{\partial w}{\partial x_i}, \tau f) + (k \frac{\partial}{\partial x_i}\frac{\partial w}{\partial x_i}, \tau f) - (sw, \tau f),
\end{aligned}
\tag{11}
$$

Where

$$
\begin{aligned}
&a_i = u_i - \frac{2C_{b2}}{\sigma \mathrm{Re}_\infty}\frac{\partial \nu_E}{\partial x_i}, s = \frac{1}{\Delta t} + \frac{2C_{w1} f_w \nu_E}{\mathrm{Re}_\infty d^2} - C_{b1}\tilde{S}, \\
&k = \frac{1}{\sigma \mathrm{Re}_\infty}(\nu + \nu_E), f = \frac{\nu_E^n}{\Delta t} - R.
\end{aligned}
\tag{12}
$$

R is defined in (8) and τ is defined as

$$
\tau = b_1^e \int_{\Omega^e} b_2^e d\Omega^e \hat{\tau} \tag{13}
$$

$$
\hat{\tau} = [(b_2^e a_i \cdot \nabla b_{1\Omega}^e) + \nabla(b_2^e \kappa \nabla, b_{\Omega}^e) + b_2^e(s_\Omega b^{-1}, \tag{14}
$$

where b_1^e is the bubble function for the trial solution and b_2^e represents the bubble for the weighting function. Further details regarding the multiscale method and the choices of bubble functions can be found from Refs. (Khurram and Masud 2006, Khurram *et al*. 2012, Masud and Khurram 2004, Masud and Khurram 2006).

3 Inflow turbulence generation

3.1 DSRFG formulation

The DSRFG inflow turbulence generation method was recently proposed by Huang, Li and Wu (2010). It is defined as a general inflow turbulence generator for unsteady numerical simulation of a spatially correlated turbulent flow field. This method is able to generate homogeneous-isotropic and inhomogeneous-anisotropic turbulence satisfying any given spectrum. Briefly, the overall velocity vector field is formed by

$$\begin{aligned}\boldsymbol{u}(\boldsymbol{x},t) &= \sum_{m=k_0}^{k_{\max}} \boldsymbol{u}_{\boldsymbol{m}}(\boldsymbol{x},t) \\ &= \sum_{m=k_0}^{k_{\max}} \sum_{n=1}^{N} \left[\boldsymbol{p}^{\boldsymbol{m,n}} \cos\left(\tilde{\boldsymbol{k}}^{\boldsymbol{m,n}} \cdot \tilde{\boldsymbol{x}} + \omega_{m,n} t\right) + \boldsymbol{q}^{\boldsymbol{m,n}} \sin\left(\tilde{\boldsymbol{k}}^{\boldsymbol{m,n}} \cdot \tilde{\boldsymbol{x}} + \omega_{m,n} t\right) \right]\end{aligned} \tag{15}$$

where

$$\boldsymbol{p}^{\boldsymbol{m,n}} = \frac{\boldsymbol{\varsigma}^{\boldsymbol{n}} \times \tilde{\boldsymbol{k}}^{\boldsymbol{m,n}}}{\left|\boldsymbol{\varsigma}^{\boldsymbol{n}} \times \tilde{\boldsymbol{k}}^{\boldsymbol{m,n}}\right|} \sqrt{a \frac{4E(k_m)}{N}}, \qquad \boldsymbol{q}^{\boldsymbol{m,n}} = \frac{\boldsymbol{\xi}^{\boldsymbol{n}} \times \tilde{\boldsymbol{k}}^{\boldsymbol{m,n}}}{\left|\boldsymbol{\xi}^{\boldsymbol{n}} \times \tilde{\boldsymbol{k}}^{\boldsymbol{m,n}}\right|} \sqrt{(1-a) \frac{4E(k_m)}{N}} \tag{16}$$

The parameters in Eqs. (15) and (16) are

$$\begin{aligned}&\boldsymbol{u} = \{u,\ v,\ w\}^{\mathrm{T}},\ \boldsymbol{x} = \{x,\ y,\ z\}^{\mathrm{T}},\ \tilde{\boldsymbol{x}} = \frac{\boldsymbol{x}}{L_s}, \tilde{\boldsymbol{k}}^{\boldsymbol{m,n}} = \frac{\boldsymbol{k}^{\boldsymbol{m,n}}}{k_0} \\ &\left|\boldsymbol{k}^{\boldsymbol{m,n}}\right| = k_m, \omega_{m,n} \in N(0, 2\pi f_m), f_m = k_m U_{avg},\end{aligned} \tag{17}$$

$\boldsymbol{\varsigma}^{\boldsymbol{n}}$ and $\boldsymbol{\xi}^{\boldsymbol{n}}$ are pseudo-random numbers following a normal distribution with mean value of 0 and standard deviation value of 1, i.e., $\boldsymbol{\varsigma}_{\boldsymbol{i}}^{\boldsymbol{n}}, \boldsymbol{\xi}_{\boldsymbol{i}}^{\boldsymbol{n}} \in N(0,1), i = 1,2,3$. $\boldsymbol{k}^{\boldsymbol{m,n}}$ is the wave number, the distribution of which is determined by the spectrum. a is uniformly distributed from 0 to 1. $E(k_m)$ is the spectrum value and N is the sampling number for each wave number k_m. L_s is a length scale of turbulence, which controls the spatial correlation. U_{avg} is the mean velocity and $\boldsymbol{k}^{\boldsymbol{m,n}}$ is isotropically distributed on the surface of a 3D sphere. In the present work it is computed by the following equations

$$\begin{cases} k_1^{m,n} = k_m \sqrt{1-b^2} \cos\alpha \\ k_2^{m,n} = k_m \sqrt{1-b^2} \sin\alpha \\ k_3^{m,n} = k_m b \end{cases} \tag{18}$$

where b and α are uniformly distributed from -1 to 1 and from 0 to 2π, respectively. Fig. 1 shows the distribution of $\boldsymbol{k}^{\boldsymbol{m,n}}$ with $k_m = 1$ and $N = 500$.

3.2 Validation of DES combined with DSRFG

The multiscale finite element DES code is implemented in FENSAP-ICE, a finite element method based Navier-Stokes solver (Aube *et al*. 2010, Beaugendre *et al*. 2006, Morency *et al*. 2001). A test case of an empty wind tunnel is presented to validate the performance of DES+ DSRFG in modeling atmospheric boundary layer flows. The dimensions of the empty wind tunnel are 2 *m*×0.4 *m*×1 *m* in *x*, *y* and *z* direction. Structured grids are used, as shown in Fig. 2, and the total node number is 526,000. The overall simulation time is 1 second, with a uniform time step of 10^{-3} second.

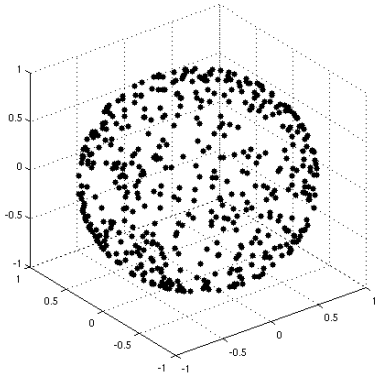

Fig. 1 Distribution of wave number $\boldsymbol{k}^{m,n}$

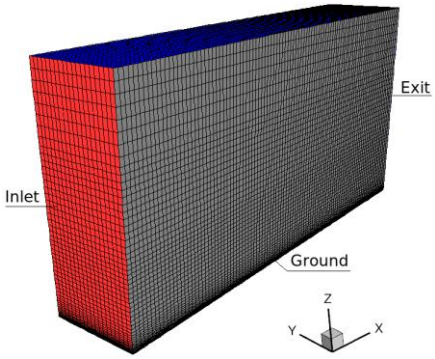

Fig. 2 Computational grid of empty wind tunnel

The inflow natural wind characteristics are assumed to follow the third flat terrain category in the Architectural Institute of Japan (AIJ) Recommendations for Loads on Buildings (AIJ 2004). The mean velocity profile and turbulence intensity profile are expressed in Eqs. (19) and (20), respectively

$$U_{avg}(z)=\begin{cases}1.0U_0\left(z_b/z_G\right)^{\alpha}, & z\le z_b\\ 1.0U_0\left(z/z_G\right)^{\alpha}, & z_b<z\le z_G\\ 1.0U_0, & z>z_G\end{cases} \tag{19}$$

$$I(z)=\begin{cases}0.1\left(z_b/z_G\right)^{(-\alpha-0.05)}, & z\le z_b\\ 0.1\left(z/z_G\right)^{(-\alpha-0.05)}, & z_b<z\le z_G\\ 0.1, & z>z_G\end{cases} \tag{20}$$

where z_b=0.02m, z_G=0.9m, α=0.2, U_0=30 (m/s). The target power spectrum density is assumed to follow von Kármán model (Simiu and Scanlan 1996)

$$S(f)=\frac{4\left(IU_{avg}\right)^2\left(L/U_{avg}\right)}{\left[1+70.8\left(fL/U_{avg}\right)^2\right]^{(5/6)}} \tag{21}$$

where L is turbulence integral length scale, and f is frequency.

The artificial inflow turbulence is calculated separately by DSRFG method. Fig. 3 presents the time history of velocity in three directions on one node at the inlet, with the duration of 1s. These instantaneous fluctuating velocities are then imposed at the inlet.

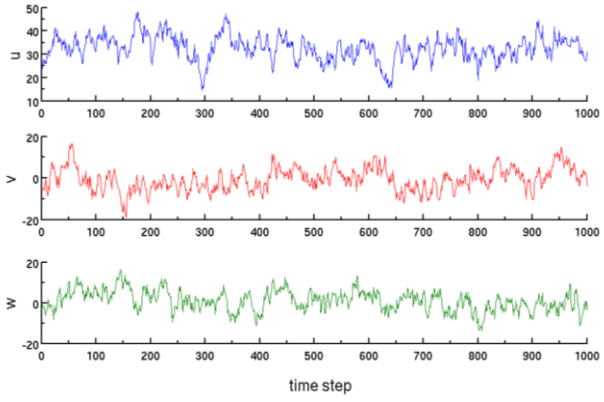

Fig. 3 Time history of velocity in three directions

Fig. 4 demonstrates an instantaneous velocity magnitude contour at inlet, middle section and exit. It is generally observed that velocity magnitudes in the flow field increase with height, and a strong stochastic phenomenon is also observed as expected.

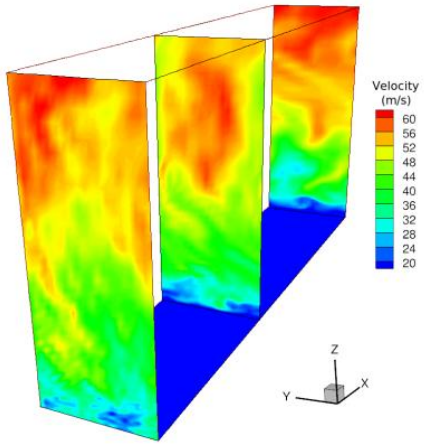

Fig. 4 Instantaneous velocity magnitude contour at inlet, middle section and exit

Statistical features are calculated to evaluate the wind field. Fig. 5 presents the comparisons of mean velocity profile and turbulence intensity profiles at inlet and exit, with the targets defined by Eqs. (19) and (20). Mean velocity and turbulence intensity are two key parameters to define wind properties. As can be seen in Fig. 5, both are in very good agreement with the targets. Moreover, Fig. 5 also indicates that the flow field is capable of maintaining the mean velocity and turbulence intensity profiles, especially for mean velocity profile, between inlet and exit. It is an important precondition for modeling flows in CWE applications.

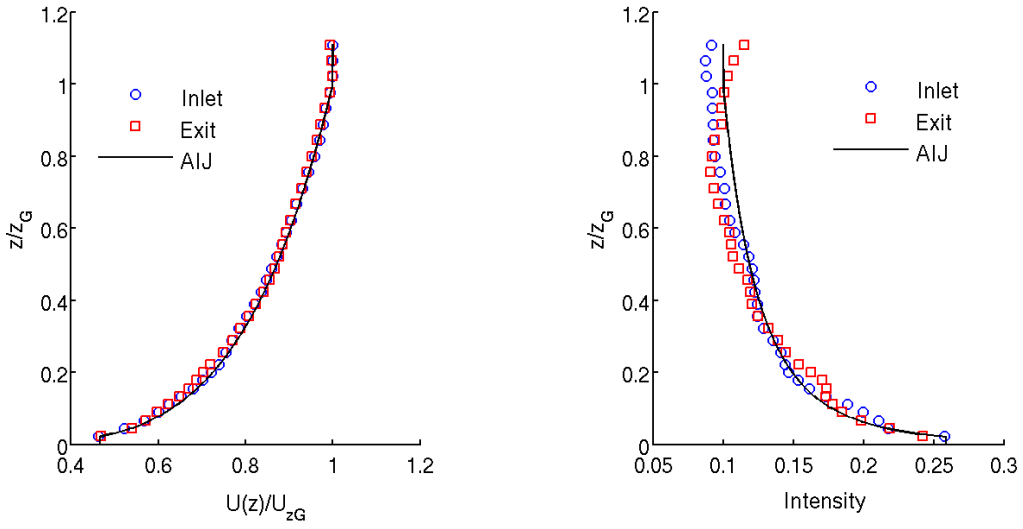

(a) Mean velocity profile (b) Turbulence intensity profile

Fig. 5 Comparisons of mean velocity and turbulence intensity profiles

Spatial correlation is also one of the most important statistical features of turbulence. If two points are very close in space, they will probably fall into the same turbulence structure with certain integral length, and therefore are more correlated. Conversely, two points farther in space will have less probability to be embedded into the same turbulence structure. The two-point spatial correlation coefficient can be determined in terms of instantaneous velocity by the following equation

$$R(i,j)=\frac{\sum_{t=1}^{n}\left(\boldsymbol{u}_{i,t}-\bar{\boldsymbol{u}}_i\right)\left(\boldsymbol{u}_{j,t}-\bar{\boldsymbol{u}}_j\right)}{\sqrt{\sum_{t=1}^{n}\left(\boldsymbol{u}_{i,t}-\bar{\boldsymbol{u}}_i\right)^2}\sqrt{\sum_{t=1}^{n}\left(\boldsymbol{u}_{j,t}-\bar{\boldsymbol{u}}_j\right)^2}} \tag{22}$$

where $\boldsymbol{u}_i$ and $\boldsymbol{u}_j$ represent the instantaneous velocity at points i and j. Shiotani and Iwatani (1976) proposed a simple formulation to estimate the lateral spatial correlation coefficient of wind, which is expressed as follows

$$R(y_i)=\exp\left(-\frac{|y_i-y_0|}{L_y}\right) \tag{23}$$

where L_y = 50 that is a constant integral scales determined experimentally. Fig. 6 shows the spatial correlation coefficient by DSRFG and by Eq. (23). The spatial correlation coefficient of DSRFG is calculated by Eq. (22) considering the velocity component in streamwise direction. It is observed that DSRFG is in good agreement with the target.

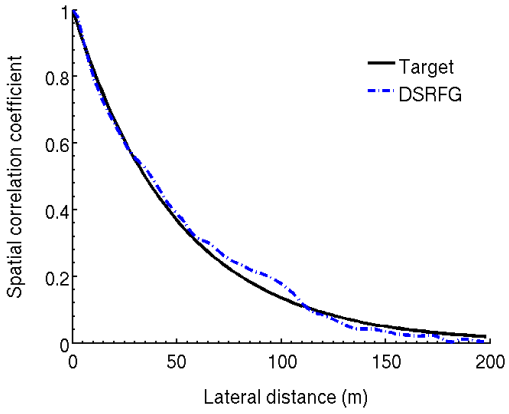

Fig. 6 Spatial correlation coefficient

Another significant property of natural wind is power spectrum density (PSD). It is found that the PSD of natural wind follows the von Kármán model defined in Eq. (21). It is clear from Fig. 7 that the PSD agrees well with von Kármán spectrum at the inlet, but misses the high frequency domain at the exit. This high frequency domain corresponds to the small eddies, which are filtered out by the grid in DES. This phenomenon is also observed in Ref. (Kataoka 2008), where an LES

method is employed along with inflow turbulence generated by recycling/rescaling method. Huang and Li (2010) believe that if the grid between the building and the inlet is fine enough, most parts of the velocity fluctuations can be resolved and made to act on the building as dynamic loads.

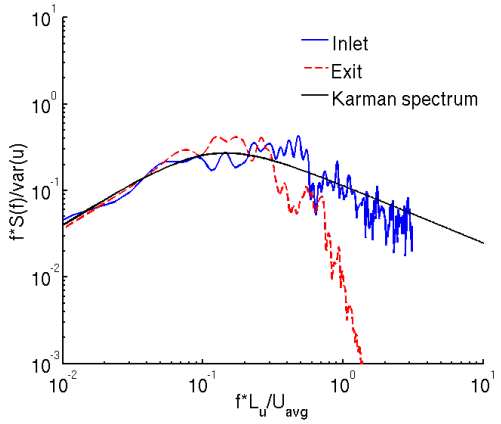

Fig. 7 Comparison of power spectrum density

Therefore, DES combined with inflow turbulence generated by DSRFG, presents an overall good modeling of atmospheric boundary layer flows. The flow field satisfies specific mean velocity and turbulence intensity profiles and shows a strong random phenomenon close to natural wind environment. Spatial correlation coefficients of turbulence are also modified to match the target formulation. For PSD analysis, it is found that the high frequency domains are absent after some distance. It is suggested to refine the grid as much as possible to circumvent this problem.

4 CAARC standard tall building model

4.1 Geometry and mesh

CAARC standard tall building model is a rectangular cylinder with width D_y = 45.72 *m*, depth D_x = 30.48 *m* and height H = 182.88 *m* as shown in Fig. 8. The blockage ratio of this numerical wind tunnel is 2.94%. A fully structured mesh consisting of 8-node hexahedral elements is employed to discretize the flow field. An internal block is placed around the building, within which the mesh is refined separately. For the boundary layer resolution, the height of first elements near the building and ground is D_y/4000 with an expansion ratio of 1.2, which ensures that most wall distances y^+ are less than unity. As suggested in Huang and Li (2010), to maintain the high frequency dynamic wind loads on building, the grid between inlet and building is also refined. Finally, 3.3×10^6 nodes are generated in the domain. Fig. 9 gives a general view of the computational mesh employed in the present study.

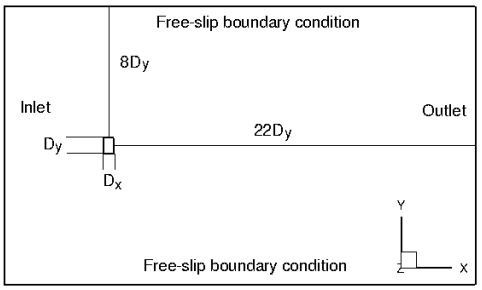

(a) Top view

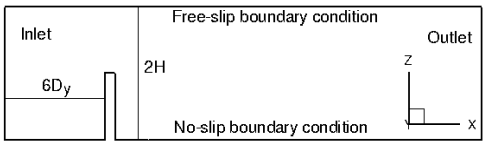

(b) X-Z central plane

Fig. 8 Computational domain and boundary conditions

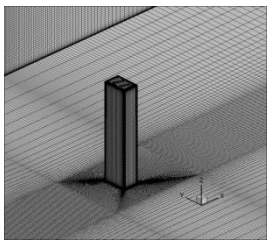

(a) Mesh around building

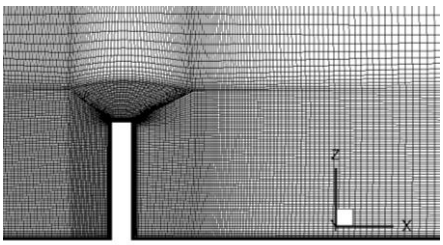

(b) X-Z central plane

Fig. 9 Computational mesh

4.2 Boundary conditions

The objective of the present work is to validate multiscale DES, combined with DSRFG technique, in predicting the pressure distribution on tall buildings under atmospheric boundary layer flows. Three test cases are simulated that are described as: 1) URANS with uniform inflow, 2) DES with uniform inflow, and 3) DES with turbulent inflow. Experiments on CAARC standard tall building model have been carried out in several wind tunnel research centers. The experimental data from the National Aeronautical Establishment (NAE) (Melbourne 1980) and University of Ottawa (Tanaka and Lawen 1986) is introduced in this paper for comparison purposes. According to these wind tunnel experiments, the velocity profile exponent α of approaching wind is suggested to be 0.28 and turbulence intensity at building height I_H is approximately 9%. Therefore, the mean velocity profile in the present numerical simulations is expressed as

$$U(z)=\begin{cases}7.447 & z\lesssim \\ 15\left(z/182.88\right)^{0.28}, & z>25\end{cases} \tag{24}$$

and the turbulence intensity in case 3 for turbulent inflow DES is assumed as

$$I(z)=\begin{cases}0.223 & z\lesssim \\ 0.065\left(z/500\right)^{-0.36}, & z>25\end{cases} \tag{25}$$

In summary, Table 1 lists the inlet boundary conditions for the present simulations and two wind tunnel experiments. Fig. 10 demonstrates the instantaneous velocity magnitude at the inlet in case 3 of DES with turbulent inflow. Strong stochastic turbulent inflow following specific mean velocity profile and turbulence intensity profile is observed.

Table 1 Description of test cases

Case	Turbulence model	Inlet boundary condition	Velocity profile exponent α	Turbulence intensity at z = H
1	Unsteady S-A RANS	Uniform inflow	0.28	0
2	DES	Uniform inflow	0.28	0
3	DES	Turbulent inflow	0.28	9 %
NAE (a)	-	Turbulent inflow	0.28	9 %
Ottawa	-	Turbulent inflow	0.28	9 %

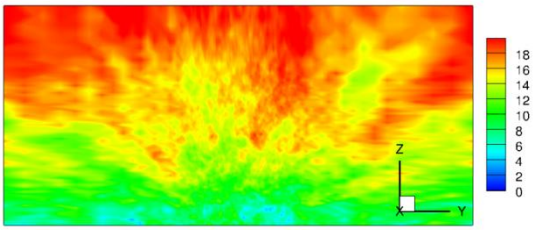

Fig. 10 Instantaneous velocity magnitude distribution at inlet in case 3 (DES with turbulent inflow)

4.3 Results and discussions

First, the time-averaged surface pressures are compared between three test cases and two wind tunnel experiments. Fig. 11 presents the time-averaged surface pressure at 2/3 building height, along the front, side and back surfaces. On the front wall, which is associated with the range $0\le X^{'}/D_x\le 1.5$ in the figure, all 3 test cases agree well with the experiments. The time-averaged

pressure on the front wall of buildings depends more on the mean velocity of the approaching wind. Therefore, no significant difference of pressure is observed since the mean velocity profiles of these test cases are similar. This is consistent with the conclusion from the LES work of Huang *et al.* (2007) that the mean pressure coefficient on the front face is insensitive to the turbulence intensity of the approaching flow, but sensitive to the velocity profile.

However, on the side and back walls, significant differences are observed between these three test cases. For case 1, URANS with S-A turbulence model, the curve of C_p seems to follow the trend of experimental data very well but obviously underestimates the values at all points. Case 2, DES with uniform inflow, overestimates the C_p, especially on the sidewall, and the curve is relatively flat indicating that the surface pressure difference at different points is insignificant, which is not the real situation. In case 3, where DES is boosted by the DSRFG turbulence inflow generation approach, the C_p distribution is much better than the other cases but still a noticeable underestimation of pressure is observed on the back wall, where turbulent flow in the wake plays an important part in the contribution of negative pressures.

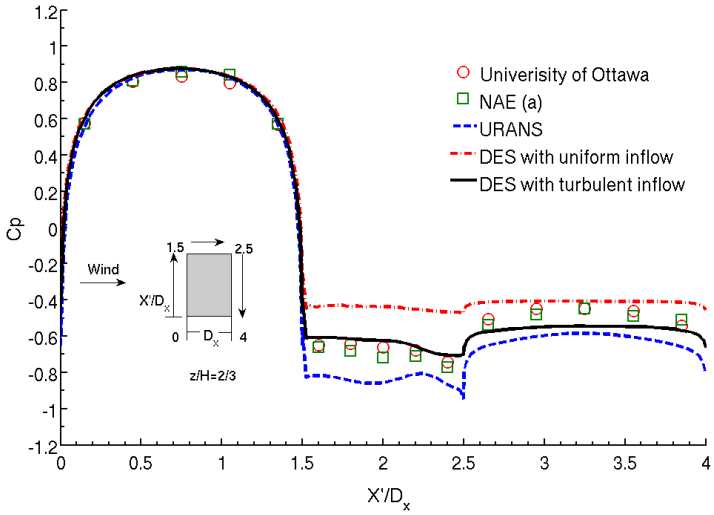

Fig. 11 Time-averaged surface pressure distribution at z =2/3H

In addition to mean flow solutions, the instantaneous flow field solutions are shown in Figs. 12 and 13. Fig. 12 exhibits the instantaneous velocity magnitude contour on the X-Z plane. The left column of Fig. 13 demonstrates the three-dimensional streamlines at 1/3 and 2/3 of the building height that starts from inlet of numerical wind tunnel, and the right column shows the streamlines at X-Z plane. As expected, the turbulence resolution in DES is very clear behind the building.

An obvious difference between DES and URANS is that the turbulent flow in DES is stochastic in the wake but URANS always presents nearly periodic behaviors. Another observation is that the building is surrounded in the atmospheric boundary layer flows as shown in case 3 (DES with turbulent inflow). This indicates that the turbulence inflow generation technique adds to the accuracy of unsteady numerical simulations by incorporating inflow turbulence that is always present in the wind tunnel experiments.

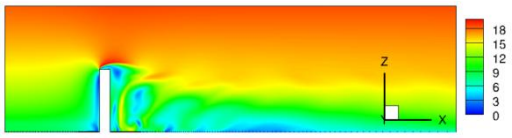

(a) URANS with uniform inflow

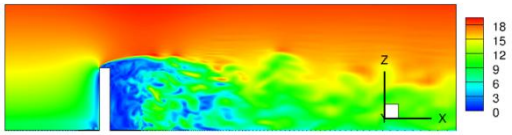

(b) DES with uniform inflow

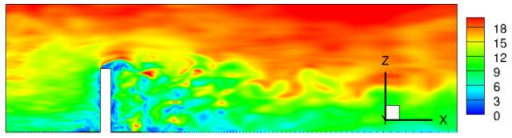

(c) DES with turbulent inflow

Fig. 12 Instantaneous velocity magnitude contour on X-Z plane

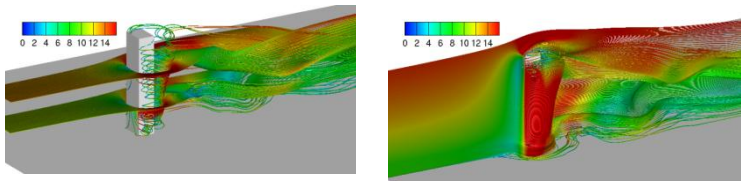

(a) URANS with uniform inflow

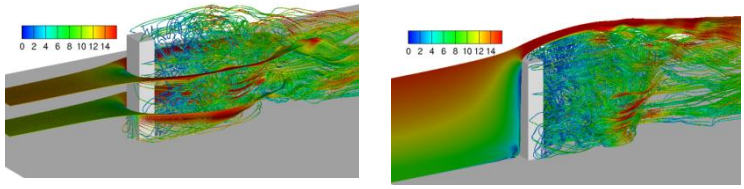

(b) DES with uniform inflow

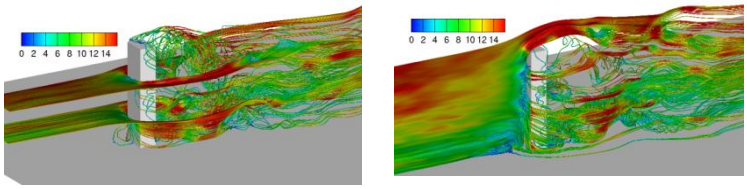

(c) DES with turbulent inflow

Fig. 13. Instantaneous streamlines colored by velocity magnitude contour

This discussion would be incomplete without a remark about the relative computational costs of URANS and DES. DES definitely requires a more refined grid than URANS in separated regions; providing more physical information but at the expense of a higher computational cost. In the present case, however, we have purposely chosen to use identical grids for the multiscale DES and URANS in order to avoid any grid influence in comparing results, and to demonstrate that URANS cannot capture turbulent features even on very fine meshes. Our conclusion is that on the same grid, the computational cost for DES and URANS is identical; in the present case: 10 seconds to complete a Newton iteration on a mesh of 3 million elements, using 16 nodes - each with 2.8 GHz dual quad-core Intel Nehalem processors.

5 Conclusions

We applied a multiscale finite element method to the Spalart-Allmaras DES formulation. The potential use of DES in CWE applications is explored by using the CAARC standard tall building model to validate DES in predicting surface pressure distributions, with DSRFG inflow turbulence generation technique to model atmospheric boundary layer flows. The main conclusions of the present work can be summarized as follows:

1. The multiscale method is applied to Spalart-Allmaras turbulence model based DES formulation. The key point of the proposed formulation is a multiscale decomposition of the scalar field into coarse and fine scales. The stabilization terms arise naturally and the method is free of user-defined stability parameters. The multiscale method provides stabilization for the convection as well as production/destruction dominated flows and, as a consequence, it demonstrates superior stability compared to artificial diffusion based methods.

2. The DSRFG inflow turbulence generation is able to model atmospheric boundary layer flows with prescribed properties. The mean velocity and turbulence intensity profiles agree well with the targets. The capability of self-sustaining these two parameters is also excellent. Spatial correlation of inflow turbulence is modified to follow specific formulation. For power spectrum density of turbulence, DSRFG follows the von Kármán spectrum well at the inlet but loses the high frequency domains after some distance. The high frequency domains are related to the small eddies that may be filtered by the grid. It is believed that finer grid will preserve them to some degree.

3. Multiscale DES under atmospheric boundary layer flows can predict closely the surface pressure distribution on the front and sidewalls of CAARC tall building model but the values on the back walls are underestimated. Compared to other two cases of URANS and DES with uniform inflow, DES with turbulent inflow presents a clear advantage in the mean pressure coefficient predictions. Three-dimensional streamlines indicate that DES can provide rich turbulence resolutions in the wake of buildings, whereas URANS always presents a periodic behavior because turbulence corresponding to all length scales is modeled. Therefore, we have successfully validated the multiscale DES in predicting surface pressure distributions on tall buildings and it is strongly suggested that turbulent inflow should also be applied in simulating unsteady flows with DES for CWE applications.

Acknowledgments

The authors would like to thank the Natural Sciences and Engineering Research Council of Canada, the Fondation Bombardier, Bombardier Aerospace, Bell Helicopter and CAE for funding through a Discovery Grant and an Industrial Research Chair.

References

Architectural Institute of Japan (2004), Recommendations for loads on buildings, Architectural Institute of Japan.

Aubé, M.S., Habashi, W.G., Wang, H.Z. and Torok, D. (2010), "On the impact of anisotropic mesh adaptation on computational wind engineering", *Int. J. Numer. Meth. Fl.*, **63**(7), 877-886.

Beaugendre, H., Morency, F. and Habashi, W.G. (2006), "Development of a second generation in-flight icing simulation code", *J. Fluid. Eng. -T ASME*, **128**, 378-387.

Braun, A.L. and Awruch, A.M. (2009), "Aerodynamic and aeroelastic analyses on the CAARC standard tall building model using numerical simulation", *Comput. Struct.*, **87**, 564-581.

Brooks, A.N. and Hughes, T.J.R. (1982), "Streamline upwind/Petrov-Galerkin formulations for convection-dominated flows with particular emphasis on the incompressible Navier-Stokes equations", *Comput. Meth. Appl. Mech. Eng.*, **32**(1-3), 199-259.

Franca, L.P., Farhat, C., Lesoinne, M. and Russo A. (1998), "Unusual stabilized finite element methods and residual free bubbles", *Int. J. Numer. Meth. Fl.*, **27** (2), 159-168.

Goliger, A.M. and Milford, R.V. (1988), "Sensitivity of the CAARC standard building model to geometric scale and turbulence", *J. Wind Eng. Ind. Aerod.*, **31**, 105-123.

Haupt, S.E., Zajaczkowski, F.J. and Peltier, L.J. (2011), "Detached eddy simulation of atmospheric flow about a surface mounted cube at high Reynolds number". *J. Fluid. Eng. -T ASME*, **133**(3), in press.

Huang, S.H. and Li, Q.S. (2010), "Large eddy simulation of wind effects on a super-tall building", *Wind Struct.*, **13**(6), 557-580.

Huang, S.H., Li, Q.S. and Wu, J.R. (2010), "A general inflow turbulence generator for large eddy simulation", *J. Wind Eng. Ind. Aerod.*, **98**, 600-617.

Huang, S.H., Li, Q.S. and Xu, S.L. (2007) "Numerical evaluation of wind effects on a tall steel building by CFD", *J. Constr. Steel Res.*, **63**, 612-627.

Hughes, T.J.R. (1995), "Multiscale phenomena: Green's functions, the Dirichlet-to-Neumann formulation, subgrid scale models, bubbles and the origins of stabilized methods", *Comput. Meth. Appl. Mech. Eng.*, **127**, 387-401.

Hughes, T.J.R., Franca, L.P. and Hulbert, G.M. (1989), "A new finite element formulation for computational fluid dynamics: VIII. The Galerkin/least-squares method for advective–diffusive equations", *Comput. Meth. Appl. Mech. Eng.*, **73**(2), 173-189.

Kataoka, H. (2008), "Numerical simulations of a wind-induced vibrating square cylinder within turbulent boundary layer", *J. Wind Eng. Ind. Aerod.*, **96**, 1985-1997.

Khurram, R.A. and Habashi, W.G. (2011), "Multiscale/Stabilized finite element method for Spalart-Allmaras turbulence model", *Proceedings of the International Conference on Finite Elements in Flow Problems. Book of Abstracts*, (Eds. Wall W. A. and Gravemeier V.), 120, Munich, Germany.

Khurram, R.A. and Masud, A. (2006), "A multiscale/stabilized formulation of the incompressible Navier-Stokes equations for moving boundary flows and fluid-structure interaction", *Comput. Mech.*, **38**, 403-416.

Khurram, R.A., Zhang, Y. and Habashi, W.G. (2012), "Multiscale finite element method applied to the Spalart-Allmaras turbulence model for 3D detached-eddy simulation", *Comp. Meth. Appl. Mech. Eng.*, (available on line) DOI: 10.1016/j.cma.2012.01.007.

Mannini, C., Soda, A. and Schewe, G. (2011), "Numerical investigation on the three-dimensional unsteady flow past a 5:1 rectangular cylinder", *J. Wind Eng. Ind. Aerod.*, **99**(4), 469-482.

Masud, A. and Khurram, R.A. (2004), "A multiscale/stabilized finite element method for the

advection-diffusion equation", *Comput. Meth. Appl. Mech. Eng*., **193**, 1997-2018.
Masud, A. and Khurram, R.A. (2006), "A multiscale finite element method for the incompressible Navier-Stokes equations", *Comput. Meth. Appl. Mech. Eng*., **195** (13-16), 1750-1777.
Melbourne, W.H. (1980), "Comparison of measurements of the CAARC standard tall building model in simulated model wind flows", *J. Wind Eng. Ind. Aerod*., **6**, 78-88.
Morency F., Beaugendre, H., Baruzzi, G.S. and Habashi, W.G. (2001), "FENSAP-ICE: A comprehensive 3D simulation tool for in-flight Icing", AIAA Paper 2001-2566, *Proceedings of the 15th AIAA Computational Fluid Dynamics Conference*, Anaheim, CA.
Murakami, S. (1998), "Overview of turbulence models applied in CWE-1997", *J. Wind Eng. Ind. Aerod*., **74-76**, 1-24.
Nozawa, K. and Tamura, T. (2002), "Large eddy simulation of the flow around a low-rise building immersed in a rough-wall turbulent boundary layer", *J. Wind Eng. Ind. Aerod*., **90**, 1151–1162.
Obasaju, E.D. (1992), "Measurement of forces and base overturning moments on the CAARC tall building model in a simulated atmospheric boundary layer", *J. Wind Eng. Ind. Aerod*., **40**, 103-126.
Shiotani. M. and Iwatani, Y. (1976), "Horizontal space correlations of velocity fluctuations during strong winds", *J. Meteorol. Soc. Jpn*., **54**, 59-67.
Simiu, E. and Scanlan, R.H. (1996), *Wind effects on structures-fundamentals and applications to design*, John Wiley & Sons, Inc., New York.
Spalart, P.R. and Allmaras, S.R. (1994), "A one-equation turbulence model for aerodynamic flows", *La Recherche Aérospatiale*, **1**, 5-21.
Spalart, P.R., Jou, W.H., Strelets, M. and Allmaras, S.R. (1997), "Comments on the feasibility of LES for wings, and on a hybrid RANS/LES approach", *Proceedings of the 1st AFOSR International Conference on DNS/LES*, (Ed. Liu, C. and Liu, Z.) Greyden, Columbus, OH. 137-147.
Tamura, T. (2008), "Towards practical use of LES in wind engineering", *J. Wind Eng. Ind. Aerod*., **96**(10-11), 1451-1471.
Tanaka, H. and Lawen, N. (1986), "Test on the CAARC standard tall building model with a length scale of 1:1000", *J. Wind Eng. Ind. Aerod*., **25**, 15-29.
Tezduyar, T.E. and Sathe S. (2007), "Modeling of fluid-structure interactions with the space-time finite elements: Solution techniques", *Int. J. Numer. Meth. Fl*., **54**, 855-900.
Tezduyar, T.E., Takizawa, K., Moorman, C.M., Wright, S. and Christopher J. (2009), "Space-time finite element computation of complex fluid-structure interactions", *Int. J. Numer. Meth. Fl*., **64**, 1201-1218.

CC